Luminescent Photoelastic Coatings

Article *in* Experimental Mechanics · August 2004

DOI: 10.1007/BF02428095

CITATIONS
21

READS
194

6 authors, including:

James P. Hubner
University of Alabama
94 PUBLICATIONS **856** CITATIONS

SEE PROFILE

Kirk S Schanze
University of Florida
404 PUBLICATIONS **15,615** CITATIONS

SEE PROFILE

Luminescent Photoelastic Coatings

Hubner, J. P.
University of Florida
PO Box 116250
Gainesville, FL 32611

Ifju, P. G.
University of Florida
PO Box 116250
Gainesville, FL 32611

Schanze, K. S.
University of Florida
PO Box 117200
Gainesville, FL 32611

Liu, Y.
University of Florida
PO Box 117200
Gainesville, FL 32611

Chen, L.
University of Florida
PO Box 116250
Gainesville, FL 32611

El-Ratal, W.
Visteon Corporation
39000 Mound Rd., Bay U-40
Sterling Hts., MI 48310-2799

ABSTRACT

This paper describes a new technique to measure the surface strain field on three-dimensional structural components under static load. The technique employs novel luminescent photoelastic coatings and digital imaging to map the in-plane strain field. The coatings consist of a binder, generally polymeric in nature, and luminescent dyes that are applied to the surface of a test part using conventional aerosol techniques. When excited with incoherent UV or blue illumination, filtered with a linear polarizer and quarter-wave plate, the corresponding emission intensity from the coating is measured via a digital camera. The relative change in emission ellipticity, both magnitude and phase as measured after passing through an analyzing polarizer, is related to the in-plane shear strain and its corresponding principal direction. This technique offers quantitative, repeatable, and high spatial resolution measurements. Additionally, it is applicable to complex three-dimensional geometries, cost efficient to implement, and suitable to be integrated in the product design cycle in conjunction with Finite Element Analysis (FEA) tools. Several basic test results are presented and discussed on metal and composite specimens to highlight various characteristics of the technology.

Nomenclature

E	=	electric field wave magnitude
h	=	coating thickness
I	=	measured emission intensity
K	=	photoelastic optical sensitivity
r	=	luminescence anisotropy
α	=	analyzer angle
γ	=	shear strain
δ	=	optical strain response, $\phi_p \sin(\Delta)$
Δ	=	relative retardation
ε	=	normal strain
θ	=	principal direction
λ	=	wavelength
ν	=	Poisson constant
ϕ	=	efficiency or attenuation

Subscripts

avg	=	average
ex	=	excitation
c	=	combined
em	=	emission
f	=	fast axis
H	=	horizontal orientation
max	=	maximum
np	=	nonpolarized
p	=	polarized
q	=	quantum
r	=	residual
s	=	slow axis
t	=	transmission or true
V	=	vertical orientation
1	=	primary in-plane principal direction
2	=	secondary in-plane principal direction
3	=	out-of-plane principal direction

Introduction

When given the task of measuring full-field, in-plane strain information on the surface of complex three-dimensional (3-D) components, whether to detect failure modes or to calibrate/validate finite element analysis (FEA) models, the number of viable experimental techniques is limited. Even fewer are applicable when using noncyclic loading (as required with thermoelastic techniques) or vibration isolation environments (as required with interferometric techniques). Additional concerns or limitations can be environmental conditions such as temperature and humidity, excessive cost, long preparation times, poor repeatability, or inadequate resolution. The latter can become an issue when the length scale of the mechanical component varies from a few centimeters to that of a few meters and the material remains in the linear deformation range. Furthermore, if a full-field strain measurement technique is to be incorporated into the design and evaluation cycle of prototypes for practical industrial applications, then results must be available in an expedient manner and compatible format.

This paper presents a new experimental stress analysis technique that measures full-field, in-plane, strain information on the surface of complex 3-D mechanical

components. The method, named Luminescent Photoelastic Coatings (LPC), is largely based on traditional photoelasticity. Photoelasticity and photoelastic coatings [1-13] have been applied to engineering problems since the 1930s with extensive contributions from many researchers. It has proven to be a valuable tool for the validation of design prototypes and the documentation of stress distributions on complex parts. The technique has been continually improved to increase its overall accuracy, ease of application, and automated data analysis. Today, there are numerous embodiments of the technology including that developed by the Photoelastic Division of the Measurements Group and Stress Photonics, Inc.

The novel LPC technique incorporates a luminescent dye either in an underlayer with a photoelastic overcoat (a dual-layer coating) or directly into the photoelastic coating itself (single-layer coating). The luminescent dye replaces the need for a reflective layer in traditional photoelastic coating techniques. The dye has been formulated to retain polarization of the illuminating field. Numerous benefits are derived by using luminescence rather than reflectance, as will be discussed in subsequent sections. Considerable effort was devoted to improving the ease of coating application by developing a spray-on, ultraviolet-cured epoxy that does not run when applied to vertical surfaces. The coating is thin (generally 100-300 μm), can typically be applied and cured within hours on small or large structural components, and contains luminescent additives to account for thickness variation. Preparation, application, and testing are performed at nominal temperature and humidity conditions typical of air-conditioned testing laboratories. An automated procedure has been developed incorporating sub-fringe analysis to alleviate the need for phase unwrapping. Data post-processing algorithms include thickness correction and residual stress (coating) correction. The theory of the method, calibration, and application to simple 2-D and complex 3-D structures are discussed in this paper.

Experimental Technique

Principle of Operation

Figure 1 shows a schematic of the basic system instrumentation. Using conventional aerosol techniques, a luminescent photoelastic coating (LPC) is applied to the specimen or component of interest. The single-layer coating incorporates the luminescent dye in a photoelastic binder. The dual-layer coating dissolves the luminescent dye in a non-photoelastic undercoat, and a photoelastic layer is applied as an overcoat. The primary advantages of the single-layer coating are faster application and thinner coatings, making it better suited for small area, high strain regions such as notches. The dual-layer coating, however, has higher signal strength and sensitivity. For either case, the coating is illuminated with ultraviolet or blue incoherent lamps. The lamps are coupled with a polarizer and quarter-wave plate (QWP: 90° phase retarder) to create circular polarized light as described by Eqs. 1a and 1b in terms of the electric field magnitude, E, for the fast and slow axes of the QWP,

$$E_f = \frac{\phi_t}{\sqrt{2}} E_{ex} \sin \omega t \qquad (1a)$$

$$E_s = \frac{\phi_t}{\sqrt{2}} E_{ex} \cos \omega t \ , \qquad (1b)$$

where ϕ_t is the transmission efficiency of polarizer and QWP pair. A strain field on the component due to an applied load is transferred to the coating, which in turn changes the stress-induced birefringence of the photoelastic layer. For a two-coat embodiment, the circularly polarized excitation, of wavelength λ_{ex}, becomes elliptically polarized as it passes through the overcoat. The novel characteristics of the luminescent undercoat are that it retains the polarization state of the excitation that has traveled through the photoelastic overcoat and then subsequently acts as a distributed diffuse light source at a higher wavelength ($\lambda_{em} > \lambda_{ex}$). This excitation is further retarded as it passes back through the overcoat. A digital camera, fitted with an analyzer optic (second linear polarizer) and a bandpass interference filter (to reject the excitation signal), measures the corresponding red-shifted emission intensity. The absorption and emission spectra for a typical formulation is shown in Fig. 2. The resulting intensity due to the polarized emission (a time-averaged integration of the electric field squared) while neglecting the angle dependence of the excitation and emission transmission through the coating is shown in Eqs. 2a and 2b:

$$I_p = \frac{\phi_t^2 \phi_q^2}{2} E_{ex}^2 \left(1 + \sin(\Delta) \sin(2\alpha - 2\theta)\right) \qquad (2a)$$

$$\Delta = \frac{2\pi K h}{\lambda^*} \gamma_{\max} \qquad (2b)$$

where ϕ_q is the quantum efficiency of luminescent undercoat, $\lambda^* = \lambda_{ex}\lambda_{em}/(\lambda_{ex}+\lambda_{em})$, and γ_{max} is the difference of the principal strains ($\varepsilon_1 - \varepsilon_2$). The intensity measured by the imager is assumed to be the sum of the polarized and nonpolarized luminescence; hence, the ratio of the measured intensity to the average measured intensity is as follows:

$$\frac{I}{I_{avg}} = 1 + \phi_p \sin(\Delta) \sin(2\alpha - 2\theta) \ , \qquad (3)$$

where the polarization efficiency, ϕ_p, is less than unity due to a contribution of the nonpolarized emission

The primary technical advantages of using a luminescent undercoat that retains polarization are:

1) a diffuse emission field on the surface of complex geometries, thus creating a more uniform spatial measurement,
2) the separation of excitation from emission, thus eliminating specular reflections via optical filtering,
3) the ability to measure off-axis regions of high incidence angle with respect to the imager optical axis, and

4) the potential use of multi-directional excitation and/or detection to decouple the individual principal strains.

Upon excitation with polarized light, the extent of luminescence polarization is described by emission anisotropy, Eqs. 4a and 4b [14].

$$r = \frac{I_{VV} - GI_{VH}}{I_{VV} + 2GI_{VH}} \quad (4a)$$

$$G = \frac{I_{HV}}{I_{HH}} \ . \quad (4b)$$

I_{XY} is the measured emission intensity with the excitation and emission polarizers adjusted to X and Y, respectively (e.g. I_{VH} represents the horizontally polarized emission intensity recorded using vertically polarized excitation). Emission anisotropy is a ratio of the polarized luminescence component to its total luminescence intensity. An anisotropy of 0.4 is expected for a randomly distributed ensemble of fluorophores that emit polarized light to the same extent as the polarized excitation. Higher values are possible when fluorophores are partially aligned. Fig. 2 is also a plot of excitation/emission anisotropy for a developed luminescent coating with good anisotropy. Values higher than zero (~0.3 as displayed for wavelengths between 500 and 700 nm) indicate the retention of polarization and the viability of the dye.

Coating Formulation and Preparation

All the experiments presented and described in this paper were performed with the two-coating formulation. The specimen or component of interest is first cleaned and degreased prior to the application of a black primer coat of 20 - 30 μm. Next, the luminescent undercoat of approximately 60 μm is sprayed over the black primer. The luminescent undercoat is formulated with a polymer binder and a dissolved luminescent dye that has the ability to retain the polarization state of the excitation energy. Candidate dyes include fluorescent dyes such as rhodamine-B, perylene diimide, courmarins, and metal complexes. The undercoat is cured at nominal room temperature and humidity (25° C and 50% RH) for approximately two hours. An epoxy-based photoelastic overcoat, incorporating bis-(4-glycidyloxyphenyl) methane (BGM) monomer, is sprayed on top of the luminescent undercoat in thin multiple layers. A thixotropic agent is included to enable the spraying on vertical surfaces without running. The application of using multiple thin layers better controls the coating thickness and minimizes the induced residual strain. The thickness of the epoxy can be intentionally varied to:

1) target the quarter-fringe value of the photoelastic overcoat, therefore, eliminating the need for phase-unwrapping and fringe counting, and
2) provide the ability to cover a wider range of strain measurement (from 50 με at the lower end to over 10,000 με at the upper end).

Nominal thickness, including the undercoat, generally is 300 μm. The epoxy overcoat is cured by subjecting the part to ultraviolet light for a short period of time at nominal room temperature and humidity. Overnight thermal curing at elevated temperatures as high as 100°C is also possible. Depending on the formulation (luminescent dye, single/dual-layer, concentration of BGM), the optical sensitivity, K, and polarization efficiency, ϕ_p, can range between 0.02 – 0.12 and 0.1 to 0.3, respectively. Thermal curing can reduce the temperature dependence of the optical sensitivity which can range from –2%/°C to –0.5%/°C.

Excitation and Imaging Equipment

Excitation sources are blue LED lamps with a center wavelength of 465 nm. The lamps were filtered with a linear polarizer and a wavelength matched quarter-wave plate. The luminescence of the LPC was monitored with 16-bit digital charged-couple device (CCD) cameras. CCD cameras are ideal imagers because of their excellent spatial (pixel) and dynamic (ratio of full-well capacity to readout noise) resolution. The cameras were fitted with a linear polarizer (analyzer), a bandpass interference filter (600 nm center wavelength), and either a Nikon standard (50 mm) or a zoom (70-210 mm) lens. The LED lamps, analyzer rotation stage, and camera were all controlled using software developed with LabVIEW. Advanced image processing and analysis tools were used in batch mode analysis to convert intensity images to full-field strain maps.

Image Acquisition and Processing

Images are acquired in a darkened testing environment to eliminate the contamination of the luminescent signal with unrelated background signals. At any given load state, including an unloaded state, a series of four images is acquired at various analyzer angles (a series of four provides a balance between measurement accuracy and measurement time). The images for the unloaded state are used to quantify residual strains inherent to the coating.

Prior to converting raw images to strain maps, the images are corrected for camera dark-field and flat-field characteristics. For a series of analyzer images at a specific load condition, the raw intensity measurements at each pixel location are numerically fitted to a sinusoidal function of the form in Eq. 3 using a nonlinear Levenberg-Marquardt numerical routine. The amplitude and phase of the sinusoidal fit are related to the magnitude of the maximum shear strain and the principal strain direction as exemplified in Fig. 3. Geometric transformations—image warping based on matching target points between loaded and unloaded conditions and performing an image-wide bilinear interpolation—are used to register the vector maps prior to subtracting the residual (unloaded state) vector map. The subtraction of the residual strain maps from the combined strain maps (loaded state), in vector form, is necessary to determine the induced strain field due to the load application only—referred to as the true strain field. In such a manner the relative retardation (hence strain

magnitude) and principal strain direction at a specific location are calculated using Eqs. 5a – 5c:

$$\Delta_t e^{i2\theta_t} = \Delta_c e^{i2\theta_c} - \Delta_r e^{i2\theta_r} \tag{5a}$$

$$\Delta_t = \sqrt{\left(\Delta_c \sin(2\theta_c) - \Delta_r \sin(2\theta_r)\right)^2 + \left(\Delta_c \cos(2\theta_c) - \Delta_r \cos(2\theta_r)\right)^2} \tag{5b}$$

$$2\theta_t = \tan 2^{-1}\left(\frac{\Delta_c \sin(2\theta_c) - \Delta_r \sin(2\theta_r)}{\Delta_c \cos(2\theta_c) - \Delta_r \cos(2\theta_r)}\right) \tag{5c}$$

Should the residual strain field of the coating be zero or negligible, the vector subtraction operation is not necessary. In addition, by converting the images to strain magnitude and direction maps prior to vector subtraction, the illumination field variation due to the relative movement of the component under load is alleviated. The amplitude component of the vector map is converted to in-plane maximum shear strain either by *a priori* (with knowledge of specific coating characteristics) or *in situ* (with corresponding strain gage data) calibration.

Description of Experiments

A variety of different experiments are presented to illustrate various aspects of the technique. These are

1) a rectangular aluminum specimen (50.8 mm by 12.6 mm cross-section) subjected to three-point bending,
2) a rectangular cantilever beam (76.2 mm by 6.3 mm cross section) with a clamped boundary condition subjected to a simple bending load,
3) a rectangular specimen (76.2 mm by 6.3 mm cross-section) with highly varying coating thickness subjected to uniaxial tension,
4) a tubular aluminum specimen (76.2 mm OD and 6.36 mm thickness) subjected to simple torsion,
5) a rectangular composite specimen (37 mm by 2.5 mm cross section) with an asymmetrical notch subjected to uniaxial tension, and
6) a 3-D, complex geometry aluminum suspension control arm of an automobile subjected to a loading configuration captured from proving ground tests.

For each test, a blue LED lamp was coupled with polarization and retardation optics to create circular polarized light. All experiments, except the control arm, used the perylene diimide-based luminescent coating. The lamp and the CCD camera (filtered with a 600 nm bandpass interference filter) were placed one to two meters from the object of interest, depending on the size of the object and the desired image resolution (generally 0.1 to 1 mm/pixel). For each experiment, a minimum of four images (α = 0°, 45°, 90°, 135°) were acquired at specific static load conditions. Coating response was calibrated with small rectangular stacked rosette gages.

Results and Discussion

Three-Point Bend Test

For the first example, a rectangular specimen is loaded in a symmetrical three-point bend apparatus as depicted in the processed results shown in Fig. 4. The upper image is a false-color representation of the maximum in-plane shear strain following a rainbow color scale (purple and blues indicate small values, greens and yellows moderate values, and oranges and reds high values). Clearly visible is the neutral axis as well as the effect of contact stress underneath the application of the load. The response is non-zero at the neutral axis and increases near the upper and lower edges due to the bending stresses. Away from the application point, the effects of contact stresses are not present, and the results match expected theoretical distributions using simple beam theory as shown in Fig. 5 for a horizontal line h/4 from the bottom of the specimen. Also shown in Fig. 4 is the corresponding principal strain direction map in terms of color field where green (center of the color legend) indicates 0° with respect to the vertical axis. Red and purple (the extremes of the color spectrum) indicate 90° CCW and 90° CW, respectively, to the vertical axis. As expected, along the compressive (top) edge, the maximum principal strain is in the vertical direction (the secondary principal strain is negative due the compression) while at the tensile (bottom) edge, the maximum principal strain is in the horizontal direction.

Simple Bending Test

Results along the centerline on the top surface of a cantilever beam subjected to a simple bending load are shown in Fig. 6. At one end of the specimen, a distributed load is applied at x = 0 mm along the width of the specimen, while at the opposite end, the specimen is clamped (x = 240 mm). Hence, along the length of the specimen, a linearly increasing moment results. This is indicated by the linearly increasing in-plane shear strain results shown in Fig. 6 for two different maximum bending moments (21.2 and 42.4 N-m). From the Poisson effect, the maximum shear strain along the length of the specimen and away from the clamped end is related to the principal strain as follows:

$$\gamma_{\max} = \varepsilon_1 - \varepsilon_2 = (1+\nu)\varepsilon_1 \ . \tag{6}$$

Near the clamped end of the specimen (within approximately one width), the shear strain results deviate away from the linear trend. This is an effect of the boundary condition presented by the clamp. At the clamp, $\varepsilon_2 \approx 0$ and Eq. 6 is no longer valid. The clamp prevents the formation of anticlastic curvature and causes the maximum shear strain to decrease compared to the trend when the secondary principal strain is not constrained.

Uniaxial Tension Test with Varying Thickness Coating

To address the coating thickness dependence of the relative retardation as shown in Eq. 2b, an osmium-based luminescent dye was added to the photoelastic overcoat. Upon excitation with the blue LED lamp, the dye emits intensity that is proportional to the thickness of the overcoat. The osmium emission is spectrally shifted from the emission of the luminescent undercoat. Images were acquired with interference bandpass filters (700 nm and

600 nm, respectively) and without the analyzer. To account for a spatially varying excitation field, the images were ratioed to each other. The corresponding ratio is proportional to thickness. This technique was applied to a rectangular specimen in which the LPC overcoat was intentionally varied between 130 μm to 300 μm.

The specimen was loaded in uniaxial tension to create a uniform strain field. In Fig. 7, the normalized shear strain results, uncorrected for coating thickness variations, demonstrate a spatially varying artificial shear strain. The relative strain-induced error is approximately 1:1 to the relative thickness error. Using the same image data as well as the thickness correction images, the thickness-induced error for the normalized strain is minimized.

Torsion Test with Stress Concentration

To provide an example of off-axis and overlapping imager measurements, a cylindrical aluminum tube with a thinned region (smaller outer diameter) was tested in pure torsion (203 and 407 N-m). Two CCD cameras were used to image the response of the LPC. The first CCD used a 50 mm lens to view the length of the specimen, and the second CCD used a zoom lens to focus on the area with decreased tubular thickness. Fig. 8 shows both the full-field shear strain results from the far-field camera as well as the shear strain measurements along the axial direction for both cameras. The full-field results show a uniform strain field, except along the thinner region where the shear strain is nearly doubled. At the junction of the two thicknesses, a region of shear relief and concentration is present in the direction from larger to smaller outer diameter. The results from the two cameras compare well with each other as indicated by the overlapping measurements (thick line/thin line) on the graph in Fig. 8.

Measurements along the circumference were relatively constant, decreasing by 5% at oblique surface angles of ±45°. The cause of the decrease (or increase in some cases) arises from the oblique propagation of excitation and emission through the coating. When traveling along a non-normal path, the effective intensity transmission, coating thickness, and in-plane strain changes. These effects are functions of the oblique angle, the coating index of refraction, and the coating Poisson ratio; thus, modifying the response equation shown in Eqs. 2a and 2b. Future research will further address and characterize these issues.

Composite Specimen Test with Stress Concentration

The first application of the LPC technique to a non-metallic surface was on a composite specimen. The rectangular specimen was fabricated using AS4/3501-6 graphite/epoxy with a 16-layer [90/0] cross-ply lay-up. A thin notch was cut into the left side of the specimen (15 mm in length) after fabrication. The specimen was loaded in uniaxial tension, and the corresponding optical strain response is shown in Fig. 9 for four load levels (890, 1780, 2670 and 3560 N). Cleary present are the vertically symmetric lobed stress concentrations, growing in size with increasing tensile load. Coating adhesion was good with no visible or detected delamination from the surface.

Control Arm Test

An aluminum suspension control arm of an automobile, supplied by Visteon Corporation, was tested [15] to provide measurements on a complex, 3-D geometry. An image of the control arm as well as processed color images of the maximum shear strain for three load conditions are shown in Fig. 10. The bushings of the control were fixed (bottom of image) while a static load was applied to the ball joint (top of image), simulating the use of the part in the vehicle. The applied load ranged between 0 to 6.67kN. A non-contact, full-field coating thickness measurement was applied using images at 600 nm and 650 nm wavelengths. Critical design areas of high shear strain for the control arm are clearly visible as indicated by the red color scale. The full-field strain maps identified and predicted a failure location which correlated with the physical durability test results of the control arm (bottom of Fig. 10). For quantitative data system repeatability purposes, the loading test was duplicated on the following day. Results at specific locations correlated to within 96%. Ref. 16 further describes the decoupling of the maximum principal strain using a Luminescent Brittle Coating (LBC) technique that is sensitive to the summation of principal strains: $\varepsilon_1 + \varepsilon_2$. Quantitative experimental results have been used by Visteon Corporation to validate and modify the analytical FEA model of the control arm by employing a iterative optimization process.

Conclusions

A new technique for measuring the maximum in-plane shear strain and corresponding principal strain direction has been developed using the principles of luminescence and photoelasticity. Several applications of the technique were presented to highlight various characteristics. The coating is sprayed onto the surface of simple or complex metallic or composite components using conventional equipment, regardless of size. The coating thickness is designed to match the expected dynamic range of the specimen under load while not exceeding the ¼-fringe value, hence removing the need for phase-unwrapping. Application requires conventional spray equipment and a few hours. The finish is hard, environmentally robust, and durable for long periods. The luminescent property of the coating provides a diffuse emission field that is red-shifted from the illumination field. This enables off-axis measurements and blockage of specular reflections. Acquisition equipment such as the digital camera, LED lamp, rotation stage, loading actuator, and strain gages are automated via computer control. Multiple camera/lamp pairs with overlapping fields-of-view are possible. Specimen preparation, data collection, and full-field strain analysis, with resolutions of 2% - 3% of the full dynamic range, can be conducted in one to two days. A darkened environment and optical access are required.

Test results from the LPC technique have been used by Visteon Corporation to detect the failure mode location of a suspension control arm and an aluminum drive shaft early on in the design stages without permanently damaging the physical prototypes. The full-field test strain data is used to establish proper boundary conditions for

FEA models. Such a testing tool represents a solution to the current trend within industry of accurately linking physical testing to analytical tools to:

1) streamline engineering processes,
2) reduce the number of prototype builds, and
3) minimize redundant and expensive physical testing without sacrificing quality.

LPC can be used in conjunction with a similar luminescent brittle coating technique to decouple the individual principal strains. Current research is focusing on decoupling the principal strains on complex geometries using information acquired solely from the LPC technique as well as expanding the technique to dynamic and high temperature applications.

Acknowledgments

The authors would like to thank Visteon Corporation – Chassis Division for their sponsorship of this research.

References

1. Coker, E. G., and Filon, L. N. G., *A Treatise on Photoelasticity*, Cambridge University Press, London 1931.
2. Frocht, M. M., *Photoelasticity*, Vol. 1, John Wiley & Sons, New York, 1941; Vol. 2, 1948.
3. Zandman, F., Redner, S., and Dally J. W., *Photoelastic Coatings*, Iowa State University Press, Ames, 1977.
4. Daily, J. W., and Riley, W. F., *Experimental Stress Analysis*, 3rd ed., McGraw-Hill, Inc., New York, 1991.
5. Oppel, G., "Polarisationsoptische Untersuchung raumlicher Spannungs-und Dehnungszustande, *Forsch. Geb. Ingenieurw*, Vol. 7, 1936, pp. 295-300.
6. Fleury, R., and Zandman, F., "Jauge D'efforts Photoelastique," *C. R. (Paris)*, Vol. 238, 1954, p. 1559.
7. D'Agostino, J., Drucker, D. C., Liu, C. K., and Mylonas, C., "Epoxy Adhesives and Casting Resins as Photo-Elastic Plastics," *Proceedings of SESA*, Vol. 12, No. 2, 1955, pp. 123-128.
8. Kawata, K., "Analysis of Elastoplastic Behavior of Metals by Means of Photoelastic Coating Method," *Journal of Sci. Res. Instrum., Tokyo*, Vol. 52, 1958, pp. 17-40.
9. Leven, M. M., "Epoxy Resins for Photoelastic Use," *Photoelasticity*, Pergamon Press, New York, 1963, pp. 145-168.
10. Ito, K., "New Model Materials for Photoelasticity and Photoplasticity," *Experimental Mechanics*, Vol. 2, No. 12, 1962, pp. 373-376.
11. Barone, S., and Patterson, E. A., "Full-field Separation of Principle Stresses by Combined Thermo- and Photoelasticity," *Experimental Mechanics*, Vol. 36, No. 4, 1996, pp. 318-324.
12. Ramesh, K., and Mangal, S. K., "Digital Acquisition Techniques in Digital Photoelasticity: A Review," *Optics and Lasers Engineering*, Vol. 30, 1998, pp. 53-75.
13. Lesniak, J. R., Zickel, M. J., Welch, C. S., and Johnson, D. F., "An Innovative Polariscope for Photoelastic Stress Analysis," *Proceedings of Society of Experimental Mechanics Conference*, June 1997.
14. Lakowicz, J. R., *Principles of Fluorescence Spectroscopy*, 2nd ed., Kluwer Academic/Plenum, New York, 1999.
15. Hubner, J. P., Ifju, P.G., Schanze, K. S., Jaing, S., Liu, Y., and El-Ratal, W., "Luminescent Strain Sensitive Coatings," AIAA Paper 2003-1437, April 2003.
16. Hubner, J. P., Ifju, P.G., Schanze, K. S., Jenkins, D. A., Carroll, B. F., Wang, Y., He, P., Brennan, A., and El-Ratal, W., "Full-field Strain Measurement using a Luminescent Coating," *Experimental Mechanics*, Vol. 43, No. 1, 2003, pp. 61-68.

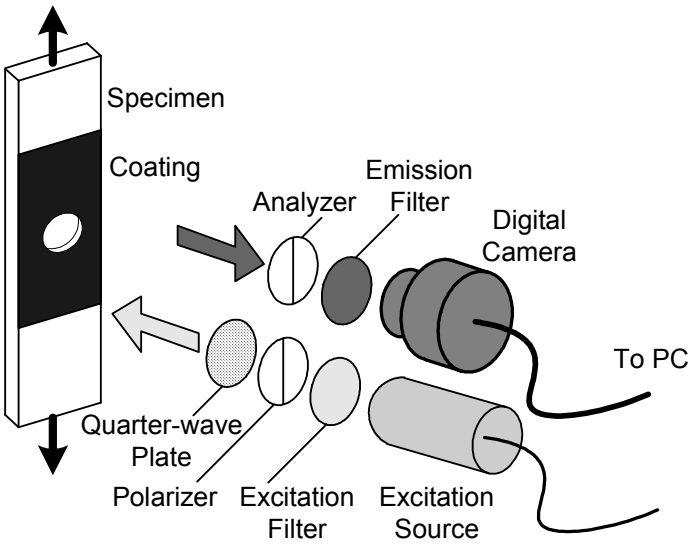

Figure 1. Schematic of basic LPC instrumentation.

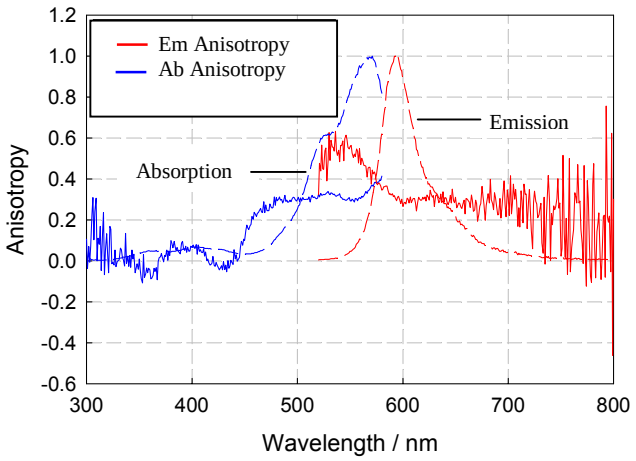

Figure 2. Absorption/emission spectra and anisotropy of a luminescent dye incorporated into an epoxy binder.

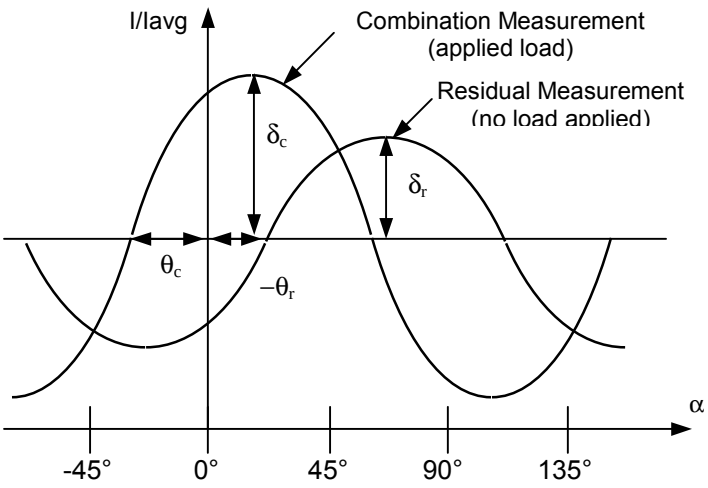

Figure 3. Theoretical intensity response of a photoelastic coating.

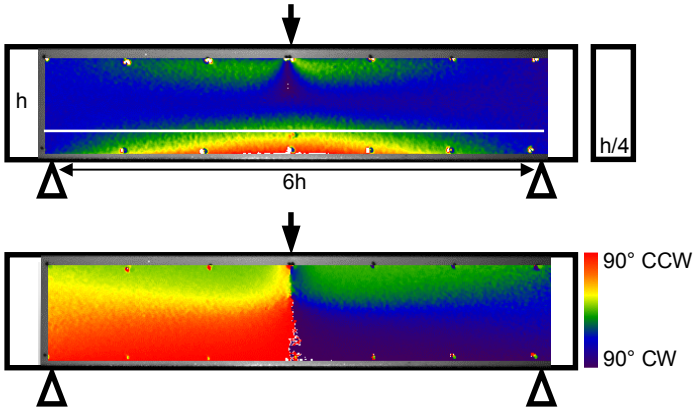

Figure 4. Side view of the optical strain response (OSR) and principal strain direction (0° vertical) for a specimen subjected to a load in a three-point bend configuration.

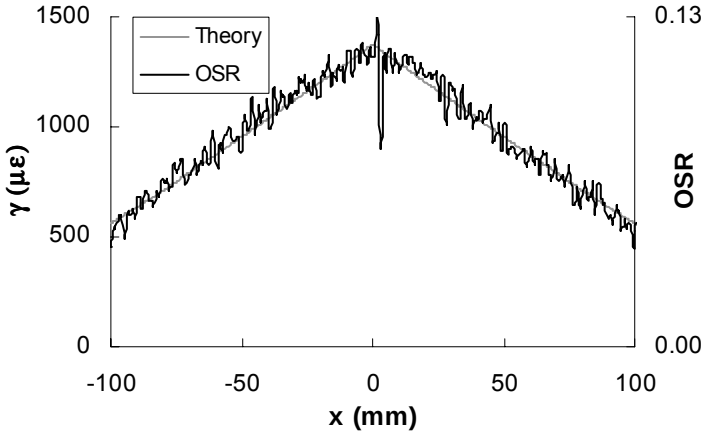

Figure 5. Comparison of OSR to calculated maximum shear strain via simple beam theory along a horizontal cut at h/4.

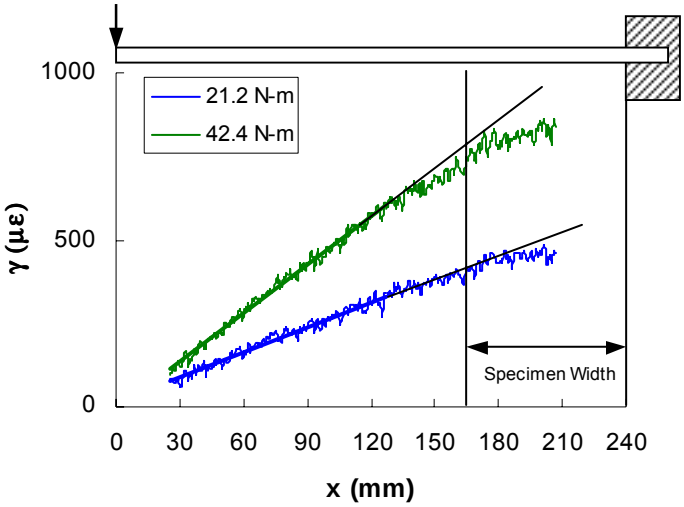

Figure 6. Maximum shear strain results along the centerline of a rectangular specimen under simple bending. Force applied at x = 0; clamped at x = 240 mm.

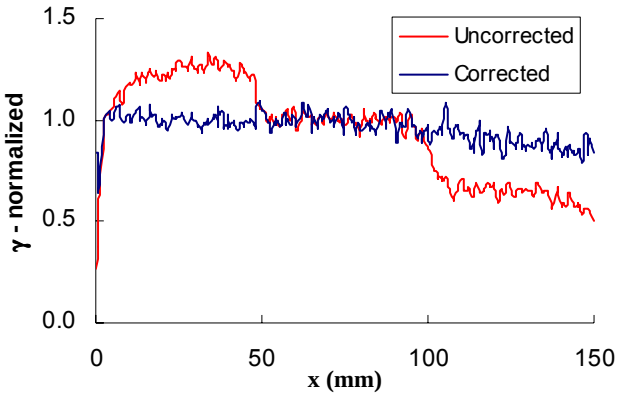

Figure 7. Thickness corrected normalized shear strain results for a rectangular specimen under uniaxial tension.

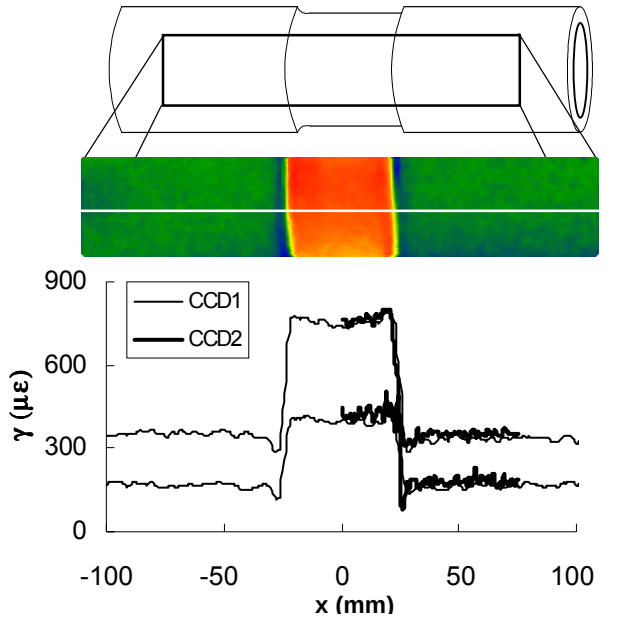

Figure 8. Maximum shear strain results on a cylindrical specimen subjected to a torsional load of 203 and 407 N-m.

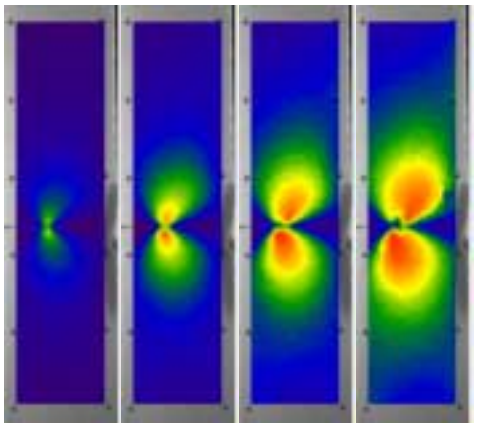

Figure 9. OSR of LPC on a composite notch specimen subjected to a uniaxial tension (890, 1780, 2670 and 3560 N).

Figure 10. Shear strain fields for the 1.3, 4.0, and 6.7 kN loading conditions (top-to-bottom).